Signals of Opportunity Aided Inertial Navigation

Joshua J. Morales, Paul F. Roysdon, and Zaher M. Kassas
University of California, Riverside

BIOGRAPHIES

Joshua J. Morales is pursuing a Ph.D. from the Department of Electrical and Computer Engineering at the University of California, Riverside. He received a B.S. in Electrical Engineering with High Honors from The University of California, Riverside. In 2016 he was accorded an Honorable Mention from the National Science Foundation. His research interests include estimation, navigation, autonomous vehicles, and intelligent transportation systems.

Paul F. Roysdon is pursuing Ph.D. and M.S. degrees from the Department of Electrical and Computer Engineering at the University of California, Riverside. He earned a B.S. in Aeronautical and Mechanical Engineering from the University of California, Davis, an M.S. in Aeronautical Engineering from the Von Karman Institute for Fluid Dynamics, Belgium, and an M.S. in Mechanical Engineering from the University of California, Davis. From 2005-2015 he was a Research Engineer in the Advanced Programs division of Composite Engineering Inc. (CEi).

Zaher (Zak) M. Kassas is an assistant professor at the University of California, Riverside and director of the Autonomous Systems Perception, Intelligence, and Navigation (ASPIN) Laboratory. He received a B.E. in Electrical Engineering from the Lebanese American University, an M.S. in Electrical and Computer Engineering from The Ohio State University, and an M.S.E. in Aerospace Engineering and a Ph.D. in Electrical and Computer Engineering from The University of Texas at Austin. From 2004 through 2010 he was a research and development engineer with the LabVIEW Control Design and Dynamical Systems Simulation Group at National Instruments Corp. His research interests include estimation, navigation, autonomous vehicles, and intelligent transportation systems.

ABSTRACT

A signal of opportunity (SOP)-aided inertial navigation system (INS) framework is presented and studied. The following problem is studied. A mobile receiver with access to global navigation satellite system (GNSS) signals is aiding its onboard INS with GNSS pseudoranges. While navigating, the receiver draws pseudorange observations on ambient unknown terrestrial SOPs and estimates the SOPs' states. GNSS signals become unavailable, at which point the receiver uses the SOPs to aid its INS. It is demonstrated that fusing SOP pseudoranges in a tightly-coupled GNSS-SOP-INS framework produces a superior navigation solution to a traditional tightly-coupled GNSS-INS framework. Moreover, in the absence of GNSS signals, it is demonstrated that aiding the INS via SOPs produces bounded estimation errors. The SOP-aided INS's performance sensitivity is studied over varying quantity and quality of exploited SOPs. Experimental results are presented demonstrating a ground vehicle navigating exclusively with inertial measurement unit (IMU) data and pseudoranges from an unknown terrestrial SOP emanating from a cellular tower.

I. INTRODUCTION

Traditional navigation systems integrate global navigation satellite system (GNSS) with an inertial navigation system (INS). When these systems are integrated, the long-term stability of a GNSS navigation solution complements the short-term accuracy of an INS. However, it is well known that if GNSS signals become unavailable, the errors of an INS diverge. Recently, signals of opportunity (SOPs) have been considered to enable navigation whenever GNSS signals become inaccessible or unreliable [1–6]. Future navigation systems could rely on SOPs to aid an INS in the absence of GNSS signals, enabling a navigation solution with bounded errors.

Architectures to fuse GNSS and inertial measurement unit (IMU) measurements with loosely-coupled, tightly-coupled, and deeply-coupled estimators, are well-studied [7]. Regardless of the coupling type, the errors of a GNSS-aided INS will diverge in the absence of GNSS signals, and the rate of divergence depends on the quality of the IMU. Consumer and small-size applications that use affordable micro-electro-mechanical systems (MEMS) grade IMUs are particularly susceptible to large error divergence rates. While high quality IMUs may reduce the rate of error divergence, they may violate cost, size, weight, and/or power constraints.

Current trends to supplement a navigation system in the event that GNSS signals become unreliable are traditionally sensor-based (e.g., cameras [8], lasers [9], and sonar [10]). Recently, SOPs (e.g., AM/FM radio [11,12], cellular [13–17], digital television [18,19], iridium [20,21], and Wi-Fi [22,23]) have been studied as a complement to GNSS or a stand-alone alternative. However, using SOPs as an aiding source for an INS received little attention. In [24], a board-mounted transceiver equipped with an IMU was presented along with experimental results demonstrating the use of SOP Doppler measurements to aid an INS. How-

Preprint of the 2016 ION GNSS+ Conference Portland, OR, September 12–16, 2016

ever, details of the framework were obscure. This paper characterizes the performance of a tightly-coupled framework that fuses IMU data with SOP pseudoranges along with GNSS pseudoranges (when available).

SOPs are transmitted at a wide range of frequencies and directions, making them an attractive supplement to GNSS signals to improve the accuracy of a navigation solution [16, 17]. SOPs are abundant in GNSS-challenged environments, making them particularly attractive aiding sources for an INS when GNSS signals become unreliable. However, unlike GNSS satellite vehicle (SV) states, the states of SOPs, namely their position and clock states, may not be known *a priori* and must be estimated. This estimation problem is analogous to the simultaneous localization and mapping (SLAM) problem in robotics [25]. Both problems ask if it is possible for an agent to start at an unknown location in an unknown environment and then to incrementally build a map of the environment while simultaneously localizing itself within this map. However, in contrast to the static environmental map of the typical SLAM problem, the SOP signal map is more complex– it is dynamic and stochastic. Specifically, for pseudorange-only observations, one must estimate not only the position states, but also the clock states of both the receiver and the SOPs [26, 27].

This paper considers the following practical problem. A mobile receiver, whether hand-held or vehicle-mounted, has access to GNSS SV observables, multiple unknown terrestrial SOPs, and IMU measurements, which are utilized to estimate the receiver's states, (position, velocity, clock bias, and clock drift) and the SOPs' states, (positions, clock biases, and clock drifts). Suddenly, GNSS pseudoranges become unavailable, and the receiver continues drawing pseudorange observations from the SOP transmitters. The receiver continues navigating by fusing the SOP pseudoranges with IMU measurements through a dynamic estimator, which simultaneously maps the SOPs' states and localizes the receiver in that map using a proposed SOP-aided INS framework. This paper studies the performance of the SOP-aided INS by addressing the following two fundamental questions on uncertainty bounds of the receiver's state estimates: (1) How are the uncertainty bounds affected by varying the number of exploited SOPs? (2) How sensitive are the uncertainty bounds to the the stability of the SOPs' oscillators?

The remainder of this paper is organized as follows. Section II describes the dynamics model of the SOPs and navigating vehicle as well as the receiver's observation model. Section III describes the SOP-aided INS framework and presents simulation results. Section IV presents a performance sensitivity analysis of the SOP-aided INS framework over varying quantity and quality of exploited SOPs. Section V presents experimental results demonstrating a ground vehicle navigating with cellular signals using the SOP-aided INS framework. Concluding remarks are given in Section VI.

II. MODEL DESCRIPTION

A. SOP Dynamics Model

Each SOP will be assumed to emanate from a spatially-stationary terrestrial transmitter, and its state vector will consist of its three-dimensional (3D) position states $\boldsymbol{r}_{\text{sop}} \triangleq [x_{\text{sop}}, y_{\text{sop}}, z_{\text{sop}}]^{\mathsf{T}}$ and clock states $\boldsymbol{x}_{\text{clk,sop}} \triangleq \left[c\delta t_{\text{sop}}, c\dot{\delta t}_{\text{sop}}\right]^{\mathsf{T}}$, where c is the speed of light, δt_{sop} is the clock bias, and $\dot{\delta t}_{\text{sop}}$ is the clock drift [28].

The SOP's discretized dynamics are given by

$$\boldsymbol{x}_{\text{sop}}(k+1) = \mathbf{F}_{\text{sop}}\,\boldsymbol{x}_{\text{sop}}(k) + \boldsymbol{w}_{\text{sop}}(k), \quad k = 1, 2, \ldots,$$

where $\boldsymbol{x}_{\text{sop}} = \left[\boldsymbol{r}_{\text{sop}}^{\mathsf{T}}, \boldsymbol{x}_{\text{clk,sop}}^{\mathsf{T}}\right]^{\mathsf{T}}$, $\mathbf{F}_{\text{sop}} = \text{diag}\left[\mathbf{I}_{3\times 3}, \mathbf{F}_{\text{clk}}\right]$, $\boldsymbol{w}_{\text{sop}}$ is the process noise, which is modeled as a discrete-time (DT) zero-mean white noise sequence with covariance $\mathbf{Q}_{\text{sop}} = \text{diag}\left[\mathbf{0}_{3\times 3}, c^2\mathbf{Q}_{\text{clk,sop}}\right]$, and

$$\mathbf{F}_{\text{clk}} = \begin{bmatrix} 1 & T \\ 0 & 1 \end{bmatrix}, \mathbf{Q}_{\text{clk,sop}} = \begin{bmatrix} S_{\tilde{w}_{\delta t_{\text{sop}}}} T + S_{\tilde{w}_{\dot{\delta t}_{\text{sop}}}} \frac{T^3}{3} & S_{\tilde{w}_{\dot{\delta t}_{\text{sop}}}} \frac{T^2}{2} \\ S_{\tilde{w}_{\dot{\delta t}_{\text{sop}}}} \frac{T^2}{2} & S_{\tilde{w}_{\dot{\delta t}_{\text{sop}}}} T \end{bmatrix},$$

where T is the constant sampling interval. The terms $S_{\tilde{w}_{\delta t_{\text{sop}}}}$ and $S_{\tilde{w}_{\dot{\delta t}_{\text{sop}}}}$ are the clock bias and drift process noise power spectra, respectively, which can be related to the power-law coefficients, $\{h_\alpha\}_{\alpha=-2}^{2}$, which have been shown through laboratory experiments to characterize the power spectral density of the fractional frequency deviation of an oscillator from nominal frequency according to $S_{\tilde{w}_{\delta t_{\text{sop}}}} \approx \frac{h_0}{2}$ and $S_{\tilde{w}_{\dot{\delta t}_{\text{sop}}}} \approx 2\pi^2 h_{-2}$ [29].

B. Vehicle Dynamics Model

The vehicle-mounted navigating receiver's state vector $\boldsymbol{x}_r$ is comprised of the INS states $\boldsymbol{x}_B$ and the receiver's clock states $\boldsymbol{x}_{\text{clk,r}} \triangleq \left[c\delta t_r, c\dot{\delta t}_r\right]^{\mathsf{T}}$, i.e., $\boldsymbol{x}_r = \left[\boldsymbol{x}_B^{\mathsf{T}}, \boldsymbol{x}_{\text{clk},r}^{\mathsf{T}}\right]^{\mathsf{T}}$.

The INS 16-state vector is

$$\boldsymbol{x}_B = \left[{}^{B}_{G}\bar{\boldsymbol{q}}^{\mathsf{T}}, \quad \boldsymbol{r}_r^{\mathsf{T}}, \quad \boldsymbol{v}_r^{\mathsf{T}}, \quad \boldsymbol{b}_g^{\mathsf{T}}, \quad \boldsymbol{b}_a^{\mathsf{T}}\right]^{\mathsf{T}},$$

where $\boldsymbol{r}_r$ and $\boldsymbol{v}_r$ are the 3-D position and velocity, respectively, of the body frame expressed in a global frame, e.g., the Earth-centered Earth-fixed (ECEF) frame; $\boldsymbol{b}_g$ and $\boldsymbol{b}_a$ are the gyroscope and accelerometer biases, respectively; and ${}^{B}_{G}\bar{\boldsymbol{q}}$ is the 4-D unit quaternion in vector-scalar form which represents the orientation of the body frame with respect to a global frame [30].

The orientation of the INS will evolve in DT according to

$${}^{B_{k+1}}_{G}\bar{\boldsymbol{q}} = {}^{B_{k+1}}_{B_k}\bar{\boldsymbol{q}} \otimes {}^{B_k}_{G}\bar{\boldsymbol{q}},$$

where ${}^{B_{k+1}}_{B_k}\bar{\boldsymbol{q}}$ represents the relative rotation in the body frame from time-step k to $k+1$, ${}^{B_k}_{G}\bar{\boldsymbol{q}}$ represents the orientation of the body frame in a global frame at time-step k, and $\otimes$ is the quaternion multiplication operator. The unit quaternion ${}^{B_{k+1}}_{B_k}\bar{\boldsymbol{q}}$ is the solution to the differential equation

$$ {}^{B_t}_{B_k}\dot{\bar{\boldsymbol{q}}} = \frac{1}{2}\begin{bmatrix} -\lfloor {}^{B}\boldsymbol{\omega}(t)\times\rfloor & {}^{B}\boldsymbol{\omega}(t) \\ -{}^{B}\boldsymbol{\omega}^{\mathsf{T}}(t) & 0 \end{bmatrix} {}^{B_t}_{B_k}\bar{\boldsymbol{q}}, \quad t \in [t_k, t_{k+1}], $$

where $t_k \triangleq kT$. The vector ${}^{B}\boldsymbol{\omega} \triangleq \left[{}^{B}\omega_x, {}^{B}\omega_y, {}^{B}\omega_z\right]^{\mathsf{T}}$ is the 3-D rotational rate vector, whereas the matrix $\lfloor {}^{B}\boldsymbol{\omega}\times\rfloor$ is the skew symmetric matrix representation of the vector ${}^{B}\boldsymbol{\omega}$. The velocity will evolve in time according to the integration

$$ \boldsymbol{v}_r(k+1) = \boldsymbol{v}_r(k) + \int_{t_k}^{t_{k+1}} {}^{G}\mathbf{a}(\tau)d\tau $$

where ${}^{G}\mathbf{a}$ is the 3-D acceleration of the IMU in the global frame. The position will evolve in time according to the integration

$$ \boldsymbol{r}_r(k+1) = \boldsymbol{r}_r(k) + \int_{t_k}^{t_{k+1}} \boldsymbol{v}_r(\tau)d\tau. $$

The evolution of $\boldsymbol{b}_g$ and $\boldsymbol{b}_a$ will be modeled as random walk processes, i.e., $\dot{\boldsymbol{b}}_a = \boldsymbol{w}_a$ and $\dot{\boldsymbol{b}}_g = \boldsymbol{w}_g$ with $\mathbb{E}[\boldsymbol{w}_g] = \mathbb{E}[\boldsymbol{w}_a] = \mathbf{0}$, $\mathrm{cov}[\boldsymbol{w}_g] = \sigma^2_{w_g}\mathbf{I}_3$, and $\mathrm{cov}[\boldsymbol{w}_a] = \sigma^2_{w_a}\mathbf{I}_3$. The above attitude, position, and velocity models are discussed in [31].

The receiver's clock states will evolve in time according to

$$ \boldsymbol{x}_{\mathrm{clk},r}(k+1) = \mathbf{F}_{\mathrm{clk}}\boldsymbol{x}_{\mathrm{clk},r}(k) + \boldsymbol{w}_{\mathrm{clk}}(k), $$

where $\boldsymbol{w}_{\mathrm{clk}}$ is the process noise vector, which is modeled as a DT zero-mean white noise sequence with covariance $\mathbf{Q}_{\mathrm{clk},r}$, which is identical to $\mathbf{Q}_{\mathrm{clk,sop}}$, except that $S_{\tilde{w}_{\delta t_{\mathrm{sop}}}}$ and $S_{\tilde{w}_{\dot{\delta} t_{\mathrm{sop}}}}$ are now replaced with receiver-specific spectra, $S_{\tilde{w}_{\delta t_r}}$ and $S_{\tilde{w}_{\dot{\delta} t_r}}$, respectively.

C. IMU Measurement Model

The IMU contains a triad-gyroscope and a triad-accelerometer which produce measurements $\boldsymbol{z}_{\mathrm{imu}} \triangleq \left[\boldsymbol{\omega}^{\mathsf{T}}_{\mathrm{imu}}, \mathbf{a}^{\mathsf{T}}_{\mathrm{imu}}\right]^{\mathsf{T}}$, which are modeled as

$$ \boldsymbol{\omega}_{\mathrm{imu}} = {}^{B}\boldsymbol{\omega} + \boldsymbol{b}_g + \boldsymbol{n}_g $$

$$ \mathbf{a}_{\mathrm{imu}} = \mathbf{R}[{}^{B_k}_{G}\bar{\boldsymbol{q}}]\left({}^{G}\mathbf{a} - {}^{G}\boldsymbol{g}\right) + \boldsymbol{b}_a + \boldsymbol{n}_a, $$

where $\mathbf{R}[\bar{\boldsymbol{q}}]$ is the equivalent rotation matrix of $\bar{\boldsymbol{q}}$, ${}^{G}\boldsymbol{g}$ is the acceleration due to gravity in the global frame, and $\boldsymbol{n}_g$ and $\boldsymbol{n}_a$ are measurement noise vectors, which are modeled as zero-mean white noise sequences with covariances $\mathbf{Q}_g$ and $\mathbf{Q}_a$, respectively.

D. Receiver Observation Model

The pseudorange observation made by the receiver on the m^{th} SOP, after discretization and mild approximations discussed in [28], is related to the receiver's and SOPs' states by

$$ \begin{aligned} z_{\mathrm{sop}_m}(j) &= \|\boldsymbol{r}_r(j) - \boldsymbol{r}_{\mathrm{sop}_m}\|_2 \\ &\quad + c\cdot\left[\delta t_r(j) - \delta t_{\mathrm{sop}_m}(j)\right] + v_{\mathrm{sop}_m}(j), \end{aligned} \tag{1} $$

where v_{sop_m} is modeled as a DT zero-mean white Gaussian sequence with variance $\sigma^2_{\mathrm{sop}_m}$. The pseudorange observation made by the receiver on the n^{th} GNSS SV, after compensating for ionospheric and tropospheric delays is related to the receiver states by

$$ \begin{aligned} z_{\mathrm{sv}_n}(j) &= \|\boldsymbol{r}_r(j) - \boldsymbol{r}_{\mathrm{sv}_n}(j)\|_2 \\ &\quad + c\cdot[\delta t_r(j) - \delta t_{\mathrm{sv}_n}(j)] + v_{\mathrm{sv}_n}(j), \end{aligned} \tag{2} $$

where, $z_{\mathrm{sv}_n} \triangleq z'_{\mathrm{sv}_n} - c\delta t_{\mathsf{iono}} - c\delta t_{\mathsf{tropo}}$, δt_{iono} and $\delta t_{\mathsf{tropo}}$ are the ionospheric and tropospheric delays, respectively, z'_{sv_n} is the uncorrected pseudorange, and $v_{\mathrm{sv_n}}$ is modeled as a DT zero-mean white Gaussian sequence with variance $\sigma^2_{\mathrm{sv_n}}$.

III. SOP-AIDED INERTIAL NAVIGATION

In this section, the SOP-aided INS framework is described and simulation results are presented to demonstrate the framework's performance in a practical scenario.

A. Problem Formulation

Consider a navigating vehicle, which is equipped with a GNSS-aided INS and a receiver capable of producing pseudoranges to M unknown SOPs. The goal of the proposed SOP-aided INS framework is twofold. First, when GNSS pseudoranges are available, SOP pseudoranges will supplement the GNSS-aided INS to improve the accuracy of the navigation solution. Second, when GNSS pseudoranges become unavailable, SOP pseudoranges will be used exclusively as an aiding source to correct the accumulating errors of the INS. To exploit SOPs for navigation, their states must be known [32–34]. However, in many practical scenarios the SOP transmitter positions are unknown. Furthermore, the SOPs' clock states are dynamic and stochastic; therefore, they must be continuously estimated. To tackle these problems, the SOP-aided INS framework will adapt a SLAM-type strategy that operates in a mapping mode when GNSS psuedoranges are available and a SLAM mode when GNSS pseudoranges are unavailable.

B. Framework

To correct INS errors using SOP pseudoranges, an extended Kalman filter (EKF) framework similar to a traditional tightly-coupled GNSS-INS integration strategy is

adopted, with the added complexity that the SOPs' states, denoted $\{\boldsymbol{x}_{\text{sop}_m}\}_{m=1}^{M}$, are simultaneously estimated alongside the navigating vehicle's states. To simplify the following discussion, consider a scenario where GNSS pseudoranges are available during $t \in [0, t_0)$ (mapping mode) and unavailable during $t \in [t_0, \infty)$ (SLAM mode), where t_0 is the instant GNSS pseudoranges become unavailable.

B.1 EKF State Model

During the mapping mode, the EKF produces an estimate $\hat{\boldsymbol{x}}(k|j) \triangleq \mathbb{E}[\boldsymbol{x}(k)|\{\boldsymbol{z}(i)\}_{i=1}^{j}]$ of $\boldsymbol{x}(k)$, and an associated estimation error covariance $\mathbf{P}_{\boldsymbol{x}}(k|j) \triangleq \mathbb{E}[\tilde{\boldsymbol{x}}(k|j)\tilde{\boldsymbol{x}}^{\mathsf{T}}(k|j)]$ where

$$\boldsymbol{x} \triangleq \left[\boldsymbol{x}_r^{\mathsf{T}},\, \boldsymbol{x}_{\text{sop}_1}^{\mathsf{T}}, \ldots, \boldsymbol{x}_{\text{sop}_M}^{\mathsf{T}}\right]^{\mathsf{T}},\ \boldsymbol{z} \triangleq \left[\boldsymbol{z}_{\text{sv}}^{\mathsf{T}},\, \boldsymbol{z}_{\text{sop}}^{\mathsf{T}}\right]^{\mathsf{T}}$$

$$\boldsymbol{z}_{\text{sv}} = \left[z_{\text{sv}_1}, \ldots, z_{\text{sv}_N}\right]^{\mathsf{T}}, \quad \boldsymbol{z}_{\text{sop}} = \left[z_{\text{sop}_1}, \ldots, z_{\text{sop}_M}\right]^{\mathsf{T}},$$

$k \geq j$, and j is the last time step an INS-aiding source was available. The EKF error state is defined as

$$\tilde{\boldsymbol{x}} \triangleq \left[\tilde{\boldsymbol{x}}_B^{\mathsf{T}},\, \tilde{\boldsymbol{x}}_{\text{clk},r}^{\mathsf{T}},\, \tilde{\boldsymbol{r}}_{\text{sop}_1}^{\mathsf{T}},\, \tilde{\boldsymbol{x}}_{\text{clk,sop}_1}^{\mathsf{T}}, \ldots, \tilde{\boldsymbol{r}}_{\text{sop}_M}^{\mathsf{T}},\, \tilde{\boldsymbol{x}}_{\text{clk,sop}_M}^{\mathsf{T}}\right]^{\mathsf{T}}, \tag{3}$$

where

$$\tilde{\boldsymbol{x}}_B = \begin{bmatrix}\tilde{\boldsymbol{\theta}}^{\mathsf{T}} & \tilde{\boldsymbol{r}}_r^{\mathsf{T}} & \tilde{\boldsymbol{v}}_r^{\mathsf{T}} & \tilde{\boldsymbol{b}}_g^{\mathsf{T}} & \tilde{\boldsymbol{b}}_a^{\mathsf{T}}\end{bmatrix}^{\mathsf{T}},$$

where $\tilde{\boldsymbol{\theta}} \in \mathbb{R}^3$ is the 3-axis error angle vector. The position, velocity, and clock errors are defined as the standard additive error, e.g., $\tilde{\boldsymbol{r}}_{\text{sop}_1} \triangleq \boldsymbol{r}_{\text{sop}_1} - \hat{\boldsymbol{r}}_{\text{sop}_1}$. The orientation error is related through the quaternion product

$${}_G^B\bar{\boldsymbol{q}} = {}_G^B\hat{\bar{\boldsymbol{q}}} \otimes \delta\bar{\boldsymbol{q}},$$

where the error quaternion $\delta\bar{\boldsymbol{q}}$ is the small deviation of the estimate ${}_G^B\hat{\bar{\boldsymbol{q}}}$ from the true orientation ${}_G^B\bar{\boldsymbol{q}}$ and is given by

$$\delta\bar{\boldsymbol{q}} = \left[\frac{1}{2}\tilde{\boldsymbol{\theta}}^{\mathsf{T}},\, \sqrt{1 - \frac{1}{4}\tilde{\boldsymbol{\theta}}^{\mathsf{T}}\tilde{\boldsymbol{\theta}}}\right]^{\mathsf{T}},$$

During the SLAM mode, $\boldsymbol{z}_{\text{sv}}$ is no longer available, therefore, the receiver's clock states $\hat{\boldsymbol{x}}_{\text{clk,r}}$ no longer need to be estimated. However, the relative biases $\Delta\delta t_m \triangleq \delta t_r - \delta t_{\text{sop}_m}$, $m = 1, ..., M$, will now be estimated. Therefore, at t_0, the states $\hat{\boldsymbol{x}}_{\text{clk,r}}$ and $\{\hat{\boldsymbol{x}}_{\text{clk,sop}_m}\}_{m=1}^{M}$ are removed from the estimator, and the relative clock state estimates $\boldsymbol{\Delta}\hat{\boldsymbol{x}}_{\text{clk}_m}$ are initialized as

$$\boldsymbol{\Delta}\hat{\boldsymbol{x}}_{\text{clk}_m} = \left[\Delta\hat{\delta}t_m, \Delta\hat{\dot{\delta}}t_m\right]^{\mathsf{T}},\ m = 1, ..., M \tag{4}$$

where

$$\Delta\hat{\delta}t_m \triangleq \hat{\delta}t_r - \hat{\delta}t_{\text{sop}_m}, \quad \Delta\hat{\dot{\delta}}t_m \triangleq \hat{\dot{\delta}}t_r - \hat{\dot{\delta}}t_{\text{sop}_m}.$$

The estimation error of the new state vector $\boldsymbol{x}'$ and the corresponding estimation error covariance are initialized according to

$$\tilde{\boldsymbol{x}}' = \mathbf{T}\tilde{\boldsymbol{x}},$$

$$\mathbf{P}_{\boldsymbol{x}'} = \mathbf{T}\mathbf{P}_{\boldsymbol{x}}\mathbf{T}^{\mathsf{T}},$$

where $\mathbf{T}$ is the transformation matrix which maps $\tilde{\boldsymbol{x}}$ from (3) to

$$\tilde{\boldsymbol{x}}' = \left[\tilde{\boldsymbol{x}}_B^{\mathsf{T}},\, \tilde{\boldsymbol{r}}_{s_1}^{\mathsf{T}},\, \boldsymbol{\Delta}\tilde{\boldsymbol{x}}_{\text{clk}_1}^{\mathsf{T}}, \ldots,\, \tilde{\boldsymbol{r}}_{s_M}^{\mathsf{T}},\, \boldsymbol{\Delta}\tilde{\boldsymbol{x}}_{\text{clk}_M}^{\mathsf{T}}\right]^{\mathsf{T}}.$$

A high-level diagram of this framework is illustrated in Fig. 1.

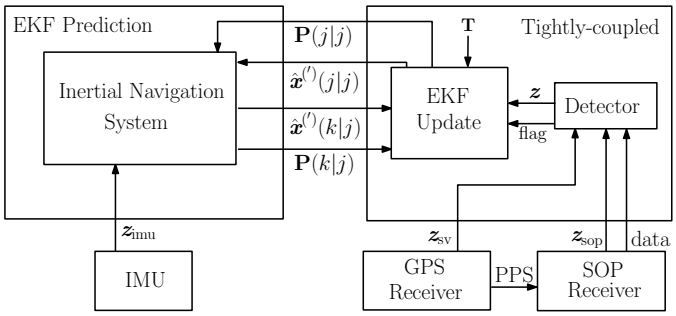

Fig. 1. SOP-aided INS framework. The flag indicates if the SOP-aided INS operates in the mapping mode: $\hat{\boldsymbol{x}}^{(\prime)} \equiv \hat{\boldsymbol{x}}$ and $\mathbf{P} \equiv \mathbf{P}_{\boldsymbol{x}}$; or the SLAM mode: $\hat{\boldsymbol{x}}^{(\prime)} \equiv \hat{\boldsymbol{x}}'$ and $\mathbf{P} \equiv \mathbf{P}_{\boldsymbol{x}'}$.

B.2 Propagation

Between aiding updates, the INS uses $\boldsymbol{z}_{\text{imu}}$ and the dynamics discussed in Section II to propagate the estimate (either $\hat{\boldsymbol{x}}$ or $\hat{\boldsymbol{x}}'$) and produce the corresponding prediction error covariance. During the mapping mode, the one-step prediction error covariance is given by

$$\mathbf{P}_{\boldsymbol{x}}(k+1|j) = \mathbf{F}\mathbf{P}_{\boldsymbol{x}}(k|j)\mathbf{F}^{\mathsf{T}} + \mathbf{Q}, \tag{5}$$

$$\mathbf{F} \triangleq \text{diag}\left[\boldsymbol{\Phi}_B,\, \mathbf{F}_{\text{clk}},\, \mathbf{F}_{\text{sop}},\, \ldots,\, \mathbf{F}_{\text{sop}}\right],$$

$$\mathbf{Q} \triangleq \text{diag}\left[\mathbf{Q}\mathbf{d}_B,\, c^2\mathbf{Q}_{\text{clk,r}},\, \mathbf{Q}_{\text{sop}},\, \ldots,\, \mathbf{Q}_{\text{sop}}\right].$$

The propagation of $\hat{\boldsymbol{x}}_B$ and calculation of the DT linearized INS state transition matrix $\boldsymbol{\Phi}_B$ and process noise covariance $\mathbf{Q}\mathbf{d}_B$ are performed through standard INS equations as described in [35, 36].

During the SLAM mode, the prediction error covariance $\mathbf{P}_{\boldsymbol{x}'}(k+1|j)$ has the same form as (5), except that $\mathbf{F}$ is replaced with $\mathbf{F}' \triangleq \text{diag}\left[\boldsymbol{\Phi}_B,\, \mathbf{F}_{\text{sop}},\, \ldots,\, \mathbf{F}_{\text{sop}}\right]$ and $\mathbf{Q}$ is replaced with $\mathbf{Q}' \triangleq \mathbf{T}\mathbf{Q}\mathbf{T}^{\mathsf{T}}$. The process noise covariance $\mathbf{Q}_{\text{clk}_m}$ of the initialized states (4) is readily shown to be $\mathbf{Q}_{\text{clk}_m} = \mathbf{Q}_{\text{clk},r} + \mathbf{Q}_{\text{clk,sop}_m}$, $m = 1, \ldots, M$.

B.3 Update

When an INS-aiding source is available, the EKF update step will correct the INS and clock errors using the standard EKF update equations [37]. In the mapping mode, i.e., $\boldsymbol{z} \triangleq \left[\boldsymbol{z}_{\text{sv}}^{\mathsf{T}},\, \boldsymbol{z}_{\text{sop}}^{\mathsf{T}}\right]^{\mathsf{T}}$, the corresponding Jacobian is

$$\mathbf{H} = \left[\mathbf{H}_{\text{sv}}^{\mathsf{T}},\, \mathbf{H}_{\text{sop}}^{\mathsf{T}}\right]^{\mathsf{T}},$$

$$\mathbf{H}_{\text{sv}} = \begin{bmatrix} \mathbf{0}_{1\times 3} & \hat{\mathbf{1}}_{\text{sv}_1}^{\mathsf{T}} & \mathbf{0}_{1\times 9} & \boldsymbol{h}_{\text{clk}}^{\mathsf{T}} & \mathbf{0}_{1\times 5M} \\ \vdots & \vdots & \vdots & \vdots & \vdots \\ \mathbf{0}_{1\times 3} & \hat{\mathbf{1}}_{\text{sv}_N}^{\mathsf{T}} & \mathbf{0}_{1\times 9} & \boldsymbol{h}_{\text{clk}}^{\mathsf{T}} & \mathbf{0}_{1\times 5M} \end{bmatrix},$$

$$\mathbf{H}_{\text{sop}} = \begin{bmatrix} \mathbf{0}_{1\times 3} & \hat{\mathbf{1}}_{\text{sop}_1}^{\mathsf{T}} & \mathbf{0}_{1\times 9} & \boldsymbol{h}_{\text{clk}}^{\mathsf{T}} & \mathbf{H}_{\text{sop}_1} & \cdots & \mathbf{0} \\ \vdots & \vdots & \vdots & \vdots & \vdots & \ddots & \vdots \\ \mathbf{0}_{1\times 3} & \hat{\mathbf{1}}_{\text{sop}_M}^{\mathsf{T}} & \mathbf{0}_{1\times 9} & \boldsymbol{h}_{\text{clk}}^{\mathsf{T}} & \mathbf{0} & \cdots & \mathbf{H}_{\text{sop}_M} \end{bmatrix},$$

where $\hat{\mathbf{1}}_{\text{sv}_n} \triangleq \frac{\hat{\boldsymbol{r}}_r - \boldsymbol{r}_{\text{sv}_n}}{\|\hat{\boldsymbol{r}}_r - \boldsymbol{r}_{\text{sv}_n}\|}$, $\boldsymbol{h}_{\text{clk}} \triangleq [1, 0]^{\mathsf{T}}$, $\hat{\mathbf{1}}_{\text{sop}_m} \triangleq \frac{\hat{\boldsymbol{r}}_r - \hat{\boldsymbol{r}}_{\text{sop}_m}}{\|\hat{\boldsymbol{r}}_r - \hat{\boldsymbol{r}}_{\text{sop}_m}\|}$, and $\mathbf{H}_{\text{sop}_m} \triangleq \left[-\hat{\mathbf{1}}_{\text{sop}_m}^{\mathsf{T}}, -\boldsymbol{h}_{\text{clk}}^{\mathsf{T}}\right]$. The update will produce the posterior estimate $\hat{\boldsymbol{x}}(j|j)$ and an associated posterior estimation error covariance $\mathbf{P}_{\boldsymbol{x}}(j|j)$.

In the SLAM mode, only SOP pseudoranges are available, i.e., $\boldsymbol{z} = \boldsymbol{z}_{\text{sop}}$. The adjusted measurement Jacobian is

$$\mathbf{H}' = \begin{bmatrix} \mathbf{0}_{1\times 3} & \hat{\mathbf{1}}_{\text{sop}_1}^{\mathsf{T}} & \mathbf{0}_{1\times 9} & \mathbf{H}'_{\text{sop}_1} & \cdots & \mathbf{0} \\ \vdots & \vdots & \vdots & \vdots & \ddots & \vdots \\ \mathbf{0}_{1\times 3} & \hat{\mathbf{1}}_{\text{sop}_M}^{\mathsf{T}} & \mathbf{0}_{1\times 9} & \mathbf{0} & \cdots & \mathbf{H}'_{\text{sop}_M} \end{bmatrix},$$

where $\mathbf{H}'_{\text{sop}_m} \triangleq \left[-\hat{\mathbf{1}}_{\text{sop}_m}^{\mathsf{T}}, \boldsymbol{h}_{\text{clk}}^{\mathsf{T}}\right]$. The update will produce the posterior estimate $\hat{\boldsymbol{x}}'(j|j)$ and an associated posterior estimation error covariance $\mathbf{P}_{\boldsymbol{x}'}(j|j)$.

C. Simulation results

In this subsection the estimation performance of the SOP-aided INS framework is analyzed using a simulator which generated (i) the "ground truth" states of the navigating vehicle, (ii) the SOPs' states, (iii) noise-corrupted IMU measurements of specific force and angular rates, and (iv) noise-corrupted pseudoranges to multiple SOPs and GPS SVs. Details of this simulator are provided next. Subsequently, estimation results produced by the SOP-aided INS are compared to estimation results produced by a traditional GPS-aided INS.

C.1 Simulator

The IMU signal generator models a triad gyroscope and a triad accelerometer. The data $y_i(t)$ for the i^{th} axis of the gyroscope and accelerometer were generated at 100Hz according to

$$y_i(t) = (1+\epsilon_{k_i})\cdot[u_i(t)+b_i(t)+\eta_{MA_i}+\eta_{Q_i}+\eta_{RRW_i}+\eta_{RR_i}],$$

where $u_i(t)$ is either the vehicle's actual acceleration or angular rotation rate for axis i, ϵ_{k_i} is the scale factor, $b_i(t)$ is a random bias which is driven by the bias instability, η_{MA_i} is the misalignment, η_Q is quantization noise, η_{RRW_i} is rate random walk, and η_{RR_i} is rate ramp [38]. The magnitude of these errors and their driving statistics are determined by the grade of the IMU. Data for a consumer-grade and tactical-grade IMU were generated for this work.

GPS L1 C/A pseudoranges were generated at 1 Hz according to (2) using SV orbits produced from Receiver Independent Exchange (RINEX) files downloaded on June 1, 2016 from a Continuously Operating Reference Station (CORS) server [39]. SOP pseudoranges were generated at 5 Hz according to (1) and the SOP dynamics discussed in Subsection II-B.

The simulated trajectory corresponded to an aerial vehicle and included two straight segments, a climb, and a repeating orbit, performed over a 200 second period. This trajectory was generated using a standard six degree of freedom (6DoF) kinematic model for airplanes [36]. Excluding trajectories generated in a closed-loop fashion so to optimize the vehicle's and SOPs' estimates [40, 41], this type of open-loop trajectory has been demonstrated to produce better estimates than an open-loop random trajectory [42, 43].

C.2 Results

Two estimation frameworks were employed to estimate the states of the navigating vehicle: (i) the SOP-aided INS equipped with a consumer-grade IMU and (ii) a traditional tightly-coupled GPS-aided INS equipped with a tactical-grade IMU. For both estimation frameworks GPS pseudoranges were set to be available for $t \in [0, 100)$, and unavailable for $t \in [100, 200]$. The initial errors of the navigating vehicle's states were initialized according to $\tilde{\boldsymbol{x}}_r(0|0) \sim \mathcal{N}[\mathbf{0}_{17\times 1}, \mathbf{P}_{\boldsymbol{x}_r}(0|0)]$, where $\mathbf{P}_{\boldsymbol{x}_r}(0|0) \equiv \text{diag}\left[(10^{-2})\cdot\mathbf{I}_{3\times 3}, 9\cdot\mathbf{I}_{3\times 3}, \mathbf{I}_{3\times 3}, (10^{-4})\cdot\mathbf{I}_{6\times 6}, 9, 1\right]$. For the SOP-aided INS framework, the SOP state estimates were initialized according to $\hat{\boldsymbol{x}}_{\text{sop}_m}(0|0) \sim \mathcal{N}\left[\boldsymbol{x}_{\text{sop}_m}(0), \mathbf{P}_{\text{sop}}(0|0)\right]$, for $m = 1, \ldots, M$, where $\boldsymbol{x}_{\text{sop}_m}(0) \equiv \left[\boldsymbol{r}_{\text{sop}_m}^{\mathsf{T}}, 10^4, 10\right]^{\mathsf{T}}$, $\mathbf{P}_{\text{sop}}(0|0) \equiv (10^4)\cdot\text{diag}\,[1, 1, 1, 0.1, 0.01]$, and the positions $\{\boldsymbol{r}_{\text{sop},m}\}_{m=1}^{M}$ were surveyed from SOP cellular tower locations in downtown Los Angeles. The simulated trajectory, SOP positions, and the position at which GPS was set to become unavailable are illustrated in Fig. 2.

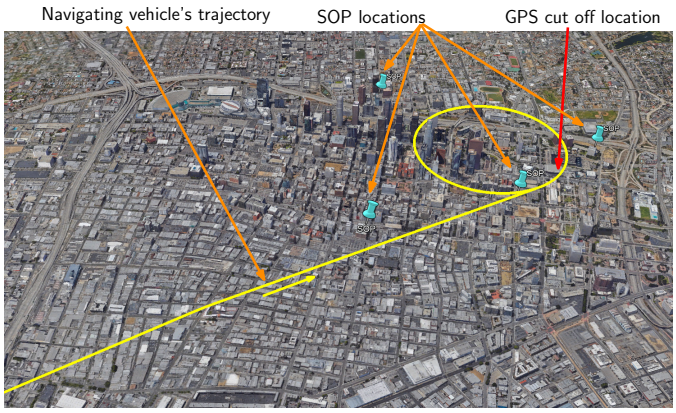

Fig. 2. True trajectory the aerial vehicle traversed (yellow) and SOP locations (blue pins).

The resulting estimation error trajectories and corresponding 3σ bounds (blue) for the position, velocity, and attitude of the receiver and the position of one of the SOPs are plotted in Figs. 3 (a)-(l). The plots in Figs. 4 (a) and (b) correspond to the estimation errors of the receiver's clock states with GPS available and the plots in Figs. 4 (c) and (d) correspond to the estimation errors of one of the SOP's clock states while GPS was available. Figs. 4 (e) and (f) correspond to the estimation errors of the relative biases and drifts that were initialized when GPS became unavailable, as was described in Subsection III-B.

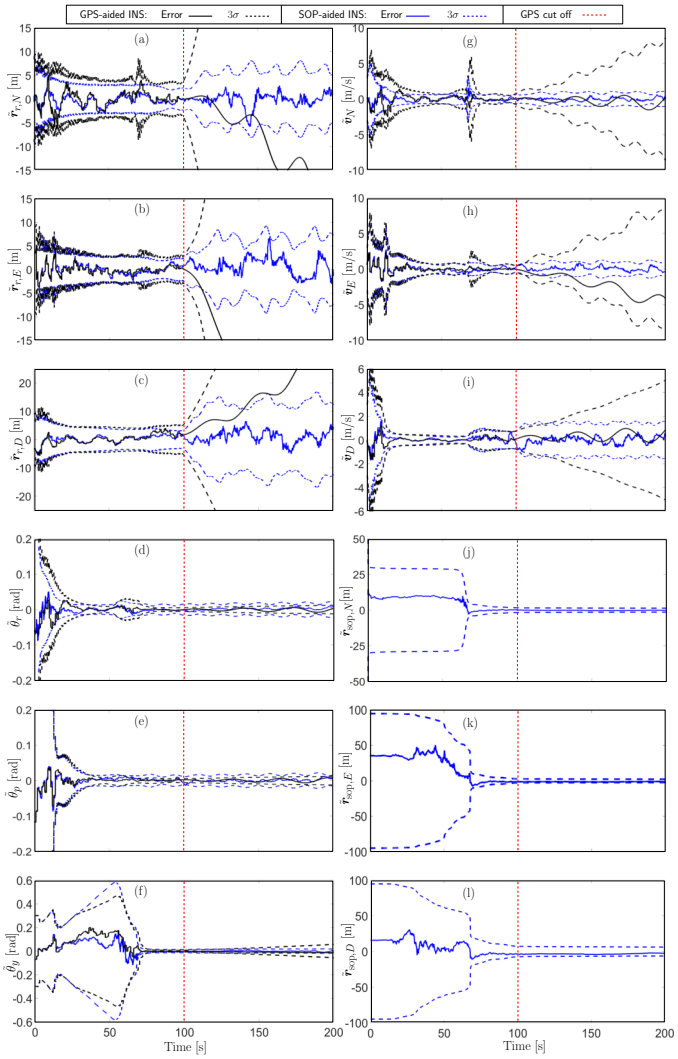

Fig. 3. The results of two simulations are illustrated. In both simulations, a navigating aerial vehicle had access to GPS pseudoranges for only the first 100 seconds while traversing the trajectory illustrated in Fig. 2. In the first simulation, a tightly-coupled GPS-INS integration strategy using a tactical-grade IMU produced the estimation error trajectories and corresponding 3σ bounds (black). In the second simulation, the SOP-aided INS framework produced the estimation error trajectories and corresponding 3σ bounds (blue). The error and 3σ bound oscillations coincide with the repeating circular path of the vehicle. North, East, and down (NED) errors are shown for position and velocity. Roll, pitch, and yaw (rpy) errors are shown for the orientation.

For a comparative analysis, the same navigating vehicle used a traditional tightly-coupled GPS-INS integration strategy with a tactical-grade IMU to estimate its states. The resulting position, velocity, and attitude estimation error trajectories and corresponding 3σ bounds (black) are plotted in Figs. 3 (a)-(i).

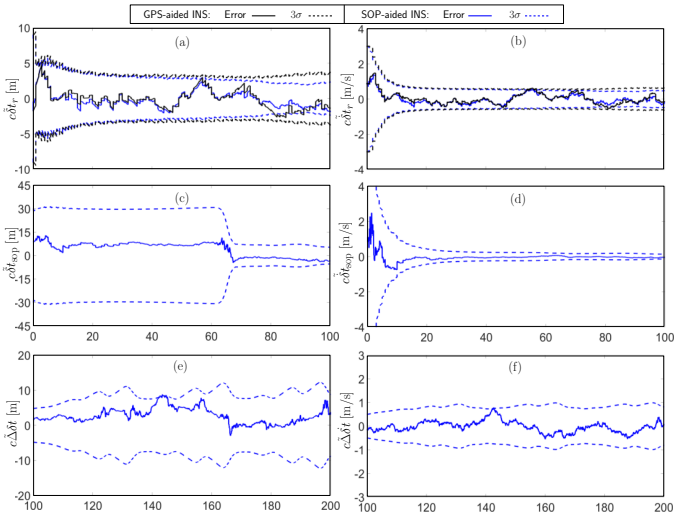

Fig. 4. Estimation error trajectories and 3σ bounds for the clock states of the SOP-aided INS framework (blue) and traditional GPS-aided INS (black). (a) and (b) correspond to the receiver's clock states while GPS was available and (c) and (d) correspond to the SOP's clock states while GPS was available. (e) and (f) correspond to $\boldsymbol{\Delta}\hat{\boldsymbol{x}}_{\text{clk}_1}$ during the SLAM mode. The 3σ bound oscillations in (e) and (f) coincide with the repeating circular path of the vehicle.

The following may be concluded from these plots. First, when GPS pseudoranges become unavailable at $t = 100$ seconds, the estimation error variances associated with the traditional GPS-INS integration strategy begin to diverge, as expected, whereas a bound can be established for the errors associated with the SOP-aided INS. Second, the SOP-aided INS with a consumer-grade IMU almost always yields lower estimation error variances when compared to the traditional GPS-INS integration strategy with a tactical-grade IMU.

IV. PERFORMANCE SENSITIVITY ANALYSIS

In the section, the performance sensitivity of the SOP-aided INS framework is studied for a varying quantity and quality of exploited SOPs.

A. Quantity of SOPs

To study the performance sensitivity of the SOP-aided INS framework over a varying number of SOPs, the states of the navigating vehicle, all available SOPs, and noise-corrupted measurements were generated using the simulator and settings described in Section III-C. Five separate simulation runs were conducted. For each simulation, the

states of the navigating vehicle were estimated. The first three runs employed the SOP-aided INS with a consumer-grade IMU and $M = 2, ..., 4$ SOPs. The last two runs, employed a traditional tightly-coupled GPS-INS integration strategy ($M = 0$) with (i) a tactical-grade IMU and (ii) a consumer-grade IMU. Fig. 5 illustrates the resulting logarithm of the determinant of the estimation error covariance for each run, which is proportional to the volume of the estimation uncertainty ellipsoid [42]. Fig. 5 (a) corresponds to the attitude ($\log\{\det[\mathbf{P}_{\bar{q}}]\}$), whereas Fig. 5 (b) corresponds to the position ($\log\{\det[\mathbf{P}_{\boldsymbol{r}_r}]\}$).

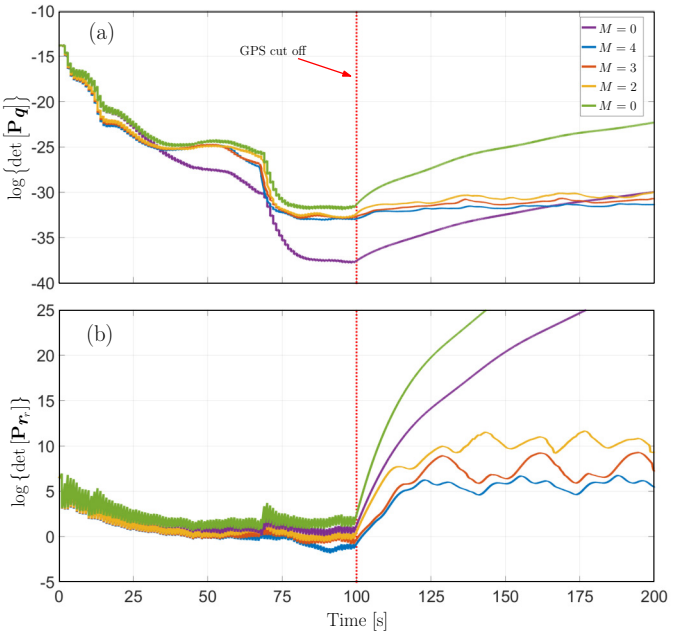

Fig. 5. An aerial navigating vehicle traverses the trajectory illustrated in Fig. 2. GPS pseudoranges become unavailable at 100s (red dotted line) and the vehicle continues to navigate by fusing INS estimates and pseudoranges from M SOPs using the framework illustrated in Fig. 1. Figures (a) and (b) correspond to the logarithm of the determinant of the estimation error covariance for attitude, and position, respectively, for exploiting a varying number of SOPs in the navigating receiver's vicinity. The two curves for $M = 0$ correspond to a traditional tightly-coupled GPS-aided INS equipped with a tactical-grade IMU (purple) and consumer-grade IMU (green).

The following may be concluded from these plots. First, the estimation uncertainties produced by the SOP-aided INS associated with both ${}^{B}_{G}\bar{\boldsymbol{q}}$ and $\boldsymbol{r}_r$ are reduced when M is increased. The sensitivity of the estimation uncertainty of ${}^{B}_{G}\bar{\boldsymbol{q}}$ and $\boldsymbol{r}_r$ to varying M is captured by the distance between the $\log\{\det[\mathbf{P}_{\bar{q}}]\}$ and $\log\{\det[\mathbf{P}_{\boldsymbol{r}_r}]\}$ trajectories, respectively. Second, although the SOP-aided INS used a consumer-grade IMU, the resulting estimation uncertainty of $\boldsymbol{r}_r$ for $M = 2, \ldots, 4$ is always lower when compared to the resulting estimation uncertainty produced by a traditional tightly-coupled GPS-INS using a tactical-grade IMU. Third, although the GPS-INS equipped with a tactical-grade IMU produces a lower estimation uncertainty of ${}^{B}_{G}\bar{\boldsymbol{q}}$ while GPS is available, the uncertainty begins to diverge when GPS becomes unavailable. This uncertainty becomes larger than the uncertainties produced by the SOP-aided INS, for which a bound may be specified for $M = 2, \ldots, 4$.

B. Quality of SOPs

In this subsection, the performance sensitivity of the SOP-aided INS framework is studied over varying qualities of SOPs. This work defines the SOP quality as the stability of the oscillator that is equipped on the SOP transmitter. The stability of the oscillator is characterized by the parameters of $\mathbf{Q}_{\text{clk,sop}}$ as described in Subsection II-A. Four simulations were conducted using the simulator and settings described in Section III-C. The resulting 3σ bounds for exploiting four SOPs, which were assumed to all be equipped with a worst temperature-compensated crystal oscillator (TCXO) (black), typical TCXO (green), typical oven-controlled crystal oscillator (OCXO) (blue), and best OCXO (purple), are plotted in Fig. 6. The four grades of oscillators considered and their characterizing parameters are tabulated in Table I.

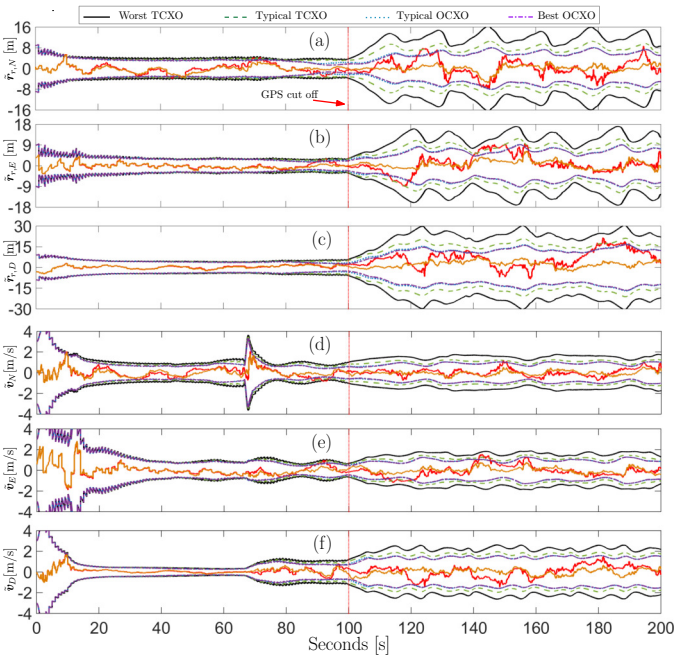

Fig. 6. An aerial navigating vehicle traverses the trajectory illustrated in Fig. 2. GPS pseudoranges become unavailable at 100s (red dotted line) and the vehicle continues to navigate using the framework illustrated in Fig. 1. Figures (a)-(f) correspond to the 3σ bounds for exploiting SOPs equipped with a worst TCXO (black), typical TCXO (green), typical OCXO (blue), and best OCXO (purple). North, East, and up (NED) position and velocity errors are shown for the worst TCXO (red) and best OCXO (orange).

From these plots it may be concluded that sensitivity of the estimation performance to the quality of oscillator was minimal while GPS was available. When GPS pseudoranges are unavailable, the estimation performance is significantly more sensitive to the quality of the oscillator,

TABLE I
QUALITY OF SOPS: OSCILLATOR TYPE

Parameter	Value
Worst TCXO $\{h_{0,s}, h_{-2,s}\}$	$\{2.0 \times 10^{-19}, 2.0 \times 10^{-20}\}$
Typical TCXO $\{h_{0,s}, h_{-2,s}\}$	$\{9.4 \times 10^{-20}, 3.8 \times 10^{-21}\}$
Typical OCXO $\{h_{0,s}, h_{-2,s}\}$	$\{8.0 \times 10^{-20}, 4.0 \times 10^{-23}\}$
Best OCXO $\{h_{0,s}, h_{-2,s}\}$	$\{2.6 \times 10^{-22}, 4.0 \times 10^{-26}\}$

and the sensitivity is captured by the distance between the 3σ trajectories. Although the uncertainty in the estimates were larger when SOPs were equipped with a worst TCXO, a bound may still be established.

V. EXPERIMENTAL RESULTS

A field experiment was conducted using an IMU and a software defined receiver (SDR) to demonstrate the SOP-aided INS framework discussed in Section III-B. To this end, two antennas were mounted on a vehicle to acquire and track multiple GPS signals and a cellular base transceiver station (BTS) whose signals were modulated through code division multiple access (CDMA). The GPS and cellular signals were simultaneously downmixed and synchronously sampled via a two-channel National Instruments® universal software radio peripheral (USRP). This front-end fed the data to the Multichannel Adaptive TRansceiver Information eXtractor (MATRIX) SDR, which produced pseudorange observables from all GPS L1 C/A signals in view, and the cellular BTS [14]. The IMU data was sampled from a navigation system developed at the University of California, Riverside (UCR), which is equipped with: (i) a consumer-grade IMU, (ii) a tactical-grade IMU, and (iii) a u-blox® GPS receiver. Fig. 7 depicts the experimental hardware setup.

Experimental results are presented for two estimators: (i) the proposed SOP-aided INS using the consumer-grade IMU and (ii) for comparative analysis, a traditional tightly-coupled GPS-INS using the consumer-grade IMU. For both estimators, GPS pseudoranges were available for only the first 16 seconds of the 30 second run. The ground truth trajectory was generated with a common GPS-INS EKF using the u-blox GPS receiver and the tactical-grade IMU. Fig. 8 is an illustration of the true and estimated vehicle trajectories, the true and estimated tower locations, and the North-East 99$^{\text{th}}$-percentile initial and final uncertainty ellipses. The North-East root mean squared error (RMSE) of the traditional tightly-coupled GPS-INS's navigation solution after GPS became unavailable was 23.5 meters. The SOP-aided INS produced a trajectory estimate with an RMSE of 9.42 meters and a final BTS localization error of 15.5 meters. Ir is worth noting that for longer periods of GPS unavailability, the RMSE reduction from the SOP-aided INS will be even more significant, since the errors of the unaided INS will diverge, while the SOP-aided INS errors are expected to remain bounded.

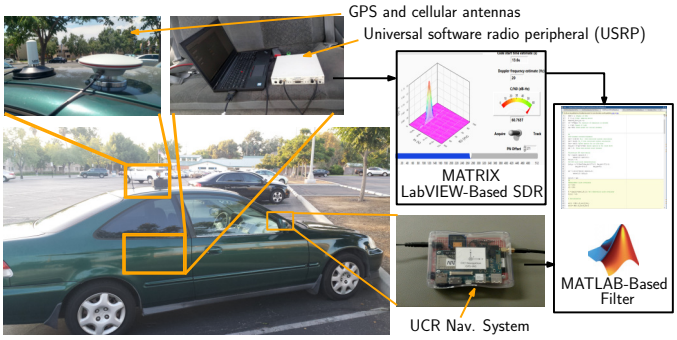

Fig. 7. Experiment hardware setup

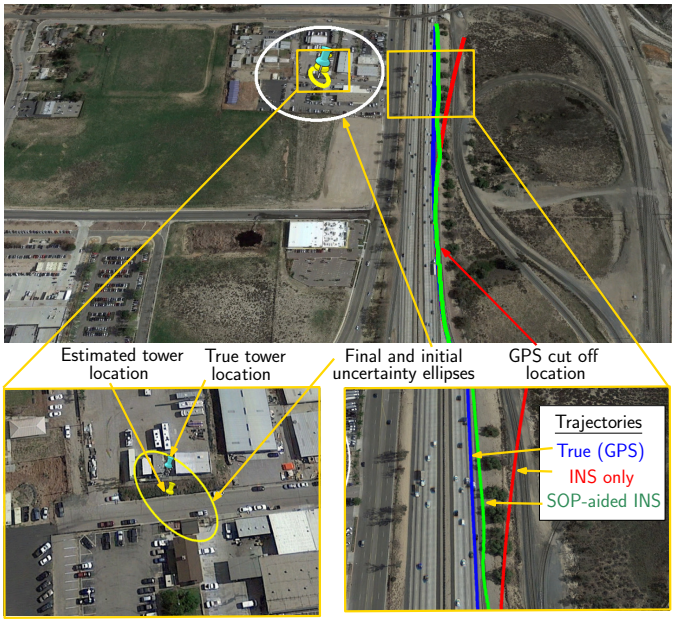

Fig. 8. Experimental results

VI. CONCLUSION

This paper presented and studied an SOP-aided INS framework. The performance of the framework was compared against a traditional tightly-coupled GNSS-INS integration strategy and the performance sensitivity was studied by varying the quantity and quality of exploited SOPs. It was demonstrated that a bound could be established on the estimation errors in the absence of GNSS. The SOP-aided INS using a consumer-grade IMU was shown to produced estimation uncertainties lower than a traditional tightly-coupled GNSS-INS using a tactical-grade IMU when two, three, or four SOPs were exploited. Furthermore, it was shown that SOPs equipped with low-quality oscillators may serve as effective INS-aiding sources to establish a bound on INS errors in the absence of

GNSS. Moreover, experimental results demonstrated a vehicle navigating with the SOP-aided INS framework in the absence of GNSS, which yielded an RMSE reduction of 59.9% when compared to an unaided INS.

Acknowledgment

This work was supported in part by the Office of Naval Research (ONR) under Grant N00014-16-1-2305. The authors would like to thank Jesse Garcia for his help with data collection.

References

[1] K. Fisher, "The navigation potential of signals of opportunity-based time difference of arrival measurements," Ph.D. dissertation, Air Force Institute of Technology, Wright-Patterson Air Force Base, Ohio, USA, 2005.

[2] J. Raquet and R. Martin, "Non-GNSS radio frequency navigation," in *Proceedings of IEEE International Conference on Acoustics, Speech and Signal Processing*, March 2008, pp. 5308–5311.

[3] L. Merry, R. Faragher, and S. Schedin, "Comparison of opportunistic signals for localisation," in *Proceedings of IFAC Symposium on Intelligent Autonomous Vehicles*, September 2010, pp. 109–114.

[4] K. Pesyna, Z. Kassas, J. Bhatti, and T. Humphreys, "Tightly-coupled opportunistic navigation for deep urban and indoor positioning," in *Proceedings of ION GNSS Conference*, September 2011, pp. 3605–3617.

[5] Z. Kassas, "Collaborative opportunistic navigation," *IEEE Aerospace and Electronic Systems Magazine*, vol. 28, no. 6, pp. 38–41, 2013.

[6] ——, "Analysis and synthesis of collaborative opportunistic navigation systems," Ph.D. dissertation, The University of Texas at Austin, USA, 2014.

[7] D. Gebre-Egziabher, "What is the difference between 'loose', 'tight', 'ultra-tight' and 'deep' integration strategies for INS and GNSS," *Inside GNSS*, pp. 28–33, January 2007.

[8] L. Mingyang and A. Mourikis, "Consistency of EKF-based visual-inertial odometry," *University of California Riverside, Tech. Rep*, 2011.

[9] A. Soloviev, "Tight coupling of GPS and INS for urban navigation," *IEEE Transactions on Aerospace and Electronic Systems*, vol. 46, no. 4, pp. 1731–1746, October 2010.

[10] G. Grenon, P. An, S. Smith, and A. Healey, "Enhancement of the inertial navigation system for the morpheus autonomous underwater vehicles," *IEEE Journal of Oceanic Engineering*, vol. 26, no. 4, pp. 548–560, October 2001.

[11] J. McEllroy, "Navigation using signals of opportunity in the AM transmission band," Master's thesis, Air Force Institute of Technology, Wright-Patterson Air Force Base, Ohio, USA, 2006.

[12] V. Moghtadaiee and A. Dempster, "Indoor location fingerprinting using FM radio signals," *IEEE Transactions on Broadcasting*, vol. 60, no. 2, pp. 336–346, June 2014.

[13] C. Yang, T. Nguyen, and E. Blasch, "Mobile positioning via fusion of mixed signals of opportunity," *IEEE Aerospace and Electronic Systems Magazine*, vol. 29, no. 4, pp. 34–46, April 2014.

[14] J. Khalife, K. Shamaei, and Z. Kassas, "A software-defined receiver architecture for cellular CDMA-based navigation," in *Proceedings of IEEE/ION Position, Location, and Navigation Symposium*, April 2016, pp. 816–826.

[15] K. Shamaei, J. Khalife, and Z. Kassas, "Performance characterization of positioning in LTE systems," in *Proceedings of ION GNSS Conference*, September 2016, accepted.

[16] J. Morales, J. Khalife, and Z. Kassas, "GNSS vertical dilution of precision reduction using terrestrial signals of opportunity," in *Proceedings of ION International Technical Meeting Conference*, January 2016, pp. 664–669.

[17] ——, "Opportunity for accuracy," *GPS World Magazine*, vol. 27, no. 3, pp. 22–29, March 2016.

[18] M. Rabinowitz and J. Spilker, Jr., "A new positioning system using television synchronization signals," *IEEE Transactions on Broadcasting*, vol. 51, no. 1, pp. 51–61, March 2005.

[19] P. Thevenon, S. Damien, O. Julien, C. Macabiau, M. Bousquet, L. Ries, and S. Corazza, "Positioning using mobile TV based on the DVB-SH standard," *NAVIGATION, Journal of the Institute of Navigation*, vol. 58, no. 2, pp. 71–90, 2011.

[20] M. Joerger, L. Gratton, B. Pervan, and C. Cohen, "Analysis of Iridium-augmented GPS for floating carrier phase positioning," *NAVIGATION, Journal of the Institute of Navigation*, vol. 57, no. 2, pp. 137–160, 2010.

[21] K. Pesyna, Z. Kassas, and T. Humphreys, "Constructing a continuous phase time history from TDMA signals for opportunistic navigation," in *Proceedings of IEEE/ION Position Location and Navigation Symposium*, April 2012, pp. 1209–1220.

[22] I. Bisio, M. Cerruti, F. Lavagetto, M. Marchese, M. Pastorino, A. Randazzo, and A. Sciarrone, "A trainingless WiFi fingerprint positioning approach over mobile devices," *IEEE Antennas and Wireless Propagation Letters*, vol. 13, pp. 832–835, 2014.

[23] J. Khalife, Z. Kassas, and S. Saab, "Indoor localization based on floor plans and power maps: Non-line of sight to virtual line of sight," in *Proceedings of ION GNSS Conference*, September 2015, pp. 2291–2300.

[24] P. MacDoran, M. Mathews, K. Gold, and J. Alvarez, "Multi-sensors, signals of opportunity augmented GPS/GNSS challenged navigation," in *Proceedings of ION International Technical Meeting Conference*, September 2013, pp. 2552–2561.

[25] H. Durrant-Whyte and T. Bailey, "Simultaneous localization and mapping: part I," *IEEE Robotics & Automation Magazine*, vol. 13, no. 2, pp. 99–110, June 2006.

[26] Z. Kassas and T. Humphreys, "Observability analysis of opportunistic navigation with pseudorange measurements," in *Proceedings of AIAA Guidance, Navigation, and Control Conference*, vol. 1, August 2012, pp. 1209–1220.

[27] ——, "Observability and estimability of collaborative opportunistic navigation with pseudorange measurements," in *Proceedings of ION GNSS Conference*, September 2012, pp. 621–630.

[28] ——, "Observability analysis of collaborative opportunistic navigation with pseudorange measurements," *IEEE Transactions on Intelligent Transportation Systems*, vol. 15, no. 1, pp. 260–273, February 2014.

[29] A. Thompson, J. Moran, and G. Swenson, *Interferometry and Synthesis in Radio Astronomy*, 2nd ed. John Wiley & Sons, 2001.

[30] N. Trawny and S. Roumeliotis, "Indirect Kalman filter for 3D attitude estimation," University of Minnesota, Dept. of Comp. Sci. & Eng., Tech. Rep. 2005-002, March 2005.

[31] M. Shelley, "Monocular visual inertial odometry," Master's thesis, Technical University of Munich, Germany, 2014.

[32] Z. Kassas and T. Humphreys, "The price of anarchy in active signal landscape map building," in *Proceedings of IEEE Global Conference on Signal and Information Processing*, December 2013, pp. 165–168.

[33] Z. Kassas, V. Ghadiok, and T. Humphreys, "Adaptive estimation of signals of opportunity," in *Proceedings of ION GNSS Conference*, September 2014, pp. 1679–1689.

[34] J. Morales and Z. Kassas, "Optimal collaborative mapping of terrestrial signals of opportunity," *IEEE Transactions on Aerospace and Electronic Systems*, 2015, in preparation.

[35] J. Farrell and M. Barth, *The Global Positioning System and Inertial Navigation*. New York: McGraw-Hill, 1998.

[36] P. Groves, *Principles of* GNSS*, Inertial, and Multisensor Integrated Navigation Systems*, 2nd ed. Artech House, 2013.

[37] Y. Bar-Shalom, X. Li, and T. Kirubarajan, *Estimation with Applications to Tracking and Navigation*. New York, NY: John Wiley & Sons, 2002.

[38] IEEE, "IEEE standard specification format guide and test procedure for linear, single-axis, non-gyroscopic accelerometers," IEEE, Tech. Rep. IEEE Std. 1293-1998 (R2008), July 2011.

[39] R. Snay and M. Soler, "Continuously operating reference station (CORS): history, applications, and future enhancements,"

Journal of Surveying Engineering, vol. 134, no. 4, pp. 95–104, November 2008.

[40] Z. Kassas, J. Bhatti, and T. Humphreys, "Receding horizon trajectory optimization for simultaneous signal landscape mapping and receiver localization," in *Proceedings of ION GNSS Conference*, September 2013, pp. 1962–1969.

[41] Z. Kassas and T. Humphreys, "Receding horizon trajectory optimization in opportunistic navigation environments," *IEEE Transactions on Aerospace and Electronic Systems*, vol. 51, no. 2, pp. 866–877, April 2015.

[42] ——, "Motion planning for optimal information gathering in opportunistic navigation systems," in *Proceedings of AIAA Guidance, Navigation, and Control Conference*, August 2013, 551–4565.

[43] Z. Kassas, A. Arapostathis, and T. Humphreys, "Greedy motion planning for simultaneous signal landscape mapping and receiver localization," *IEEE Journal of Selected Topics in Signal Processing*, vol. 9, no. 2, pp. 247–258, March 2015.